This item is likely protected under Title 17 of the U.S. Copyright Law. Unless on a Creative Commons license, for uses protected by Copyright Law, contact the copyright holder or the author.

Access to this work was provided by the University of Maryland, Baltimore County (UMBC) ScholarWorks@UMBC digital repository on the Maryland Shared Open Access (MD-SOAR) platform.

Please provide feedback

Please support the ScholarWorks@UMBC repository by emailing scholarworks-group@umbc.edu and telling us what having access to this work means to you and why it's important to you. Thank you.

The Astrophysical Journal, 861:113 (12pp), 2018 July 10 https://doi.org/10.3847/1538-4357/aac772
© 2018. The American Astronomical Society. All rights reserved.

Astrometric Limits on the Stochastic Gravitational Wave Background

Jeremy Darling, Alexandra E. Truebenbach, and Jennie Paine
Center for Astrophysics and Space Astronomy, Department of Astrophysical and Planetary Sciences, University of Colorado, 389 UCB Boulder, CO 80309-0389, USA; jeremy.darling@colorado.edu
Received 2017 October 25; revised 2018 May 5; accepted 2018 May 17; published 2018 July 11

Abstract

The canonical methods for gravitational wave detection are ground- and space-based laser interferometry, pulsar timing, and polarization of the cosmic microwave background. But as has been suggested by numerous investigators, astrometry offers an additional path to gravitational wave detection. Gravitational waves deflect light rays of extragalactic objects, creating apparent proper motions in a quadrupolar (and higher-order modes) pattern. Astrometry of extragalactic radio sources is sensitive to gravitational waves with frequencies between roughly 10^{-18} and 10^{-8} Hz (H_0 and $1/3$ yr^{-1}), overlapping and bridging the pulsar timing and CMB polarization regimes. We present a methodology for astrometric gravitational wave detection in the presence of large intrinsic uncorrelated proper motions (i.e., radio jets). We obtain 95% confidence limits on the stochastic gravitational wave background using 711 radio sources, $\Omega_{\rm GW} < 0.0064$, and using 508 radio sources combined with the first *Gaia* data release: $\Omega_{\rm GW} < 0.011$. These limits probe gravitational wave frequencies 6×10^{-18} Hz $\lesssim f \lesssim 1 \times 10^{-9}$ Hz. Using a *WISE-Gaia* catalog of 567,721 AGN, we predict a limit expected from *Gaia* alone of $\Omega_{\rm GW} < 0.0006$, which is significantly higher than was originally forecast. Incidentally, we detect and report on 22 new examples of optical superluminal motion with redshifts 0.13–3.89.

Key words: astrometry – cosmology: observations – gravitational waves – inflation – proper motions – techniques: high angular resolution

Supporting material: machine-readable tables

1. Introduction

A stochastic gravitational wave background deflects light from distant objects, producing an apparent proper motion (Braginsky et al. 1990). The angular deflections will be correlated across the sky with an amplitude of the order of the dimensionless strain of the gravitational waves, $h_{\rm rms}$ (Braginsky et al. 1990; Kaiser & Jaffe 1997); one microarcsecond (μas) of deflection is equivalent to a dimensionless strain $h \sim 5 \times 10^{-12}$. Observations spanning a time interval $\Delta t = 1/f_{\rm obs}$ will be sensitive to gravitational waves with frequencies $f < f_{\rm obs}$, roughly down to the inverse of the light travel time to the observed objects, $f \sim 10^{-18}$–10^{-17} Hz (e.g., Book & Flanagan 2011).

Book & Flanagan (2011) show that the cosmological gravitational wave background energy density can be related to the correlated light deflections as

$$\Omega_{\rm GW}(f) \sim \langle \mu(f)^2 \rangle / H_0^2, \quad (1)$$

where $\langle \mu(f)^2 \rangle$ is the variance in the proper motion at observed frequency f, and H_0 is the Hubble constant. The proper motion power spectrum, for quadrupolar and higher-order modes, can measure or constrain the gravitational wave background over 10 decades in frequency, $H_\circ \lesssim f \lesssim 1$ yr^{-1} ($10^{-18} \lesssim f \lesssim 10^{-8}$ Hz). The dominant signal is quadrupolar (Figure 1), with smaller contributions from $\ell > 2$ modes. In practice, observations constrain the energy density integrated over frequencies, $\int \Omega_{\rm GW}(f) d \ln f$, which will hereafter be labeled as $\Omega_{\rm GW}$.

Detecting or constraining $\sim 10^{-18}$–10^{-16} Hz primordial gravitational waves is a key goal of CMB polarization *B*-mode measurements (e.g., Kamionkowski et al. 1997; Seljak & Zaldarriaga 1997; Ishino et al. 2016), but between the CMB polarization measurements and pulsar timing, which is sensitive to frequencies $\sim 10^{-9}$–10^{-7} Hz (e.g., Arzoumanian et al. 2016), are $\sim$7 orders of magnitude in frequency space. Proper motion measurements can approach gravitational wave detection in a completely independent manner and bridge the frequency gap between the pulsar timing and CMB polarization methods. The frequency range $f \gtrsim 10^{-15}$ Hz can also be probed using the CMB power spectrum because gravitational waves contribute to the radiation density of the universe and can mimic a massless neutrino, modifying the effective number of neutrino species (e.g., Smith et al. 2006).

Previous observational work on astrometric detection of gravitational waves using active galactic nuclei (AGNs) using radio interferometry include Gwinn et al. (1997) and Titov et al. (2011). They quote upper limits on the stochastic gravitational wave background—expressed in terms of the critical cosmological energy density—of $\Omega_{\rm GW} < 0.11\ h_{100}^{-2}$ for $f < 2 \times 10^{-9}$ Hz at 95% confidence (Gwinn et al. 1997) and $\Omega_{\rm GW} < 0.0042\ h_{100}^{-2}$ for $f < 10^{-9}$ Hz (Titov et al. 2011). However, we cannot reproduce either of these limits based on their quoted quadrupolar fit parameters.

In this paper, we present detailed methods for astrometric measurement of the gravitational wave background including a maximum likelihood method for extracting correlated signals in vector fields with large significant outliers (the uncorrelated "intrinsic" apparent proper motion induced by relativistic jets; Section 2). We use these methods in Sections 3–5 to obtain new stochastic gravitational wave limits from a Very Long Baseline Array (VLBA)[1] astrometric catalog (Truebenbach & Darling 2017) and from this catalog combined with the first *Gaia* data release (Gaia Collaboration et al. 2016a, 2016b). We also use a *Gaia-WISE* catalog (Paine et al. 2018) to make

[1] The National Radio Astronomy Observatory is a facility of the National Science Foundation operated under cooperative agreement by Associated Universities, Inc.

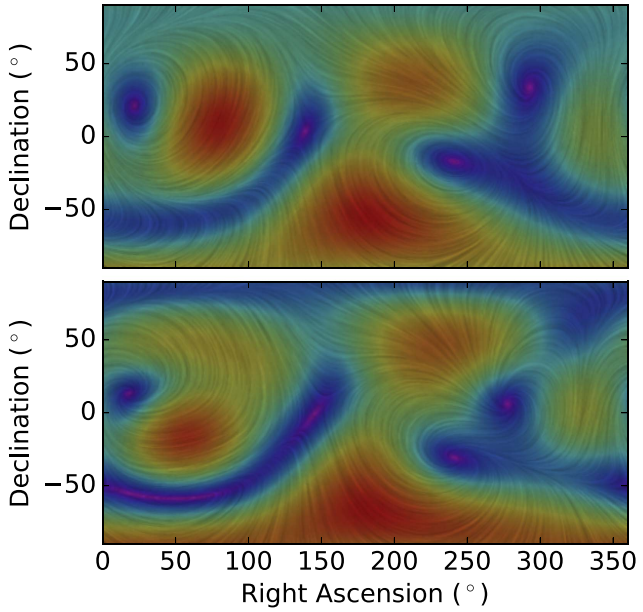

Figure 1. Randomly generated all-sky quadrupole (top) and quadrupole plus octopole (bottom) *E*- and *B*-mode stream plots in equatorial coordinates (see Section 2). For the combined quadrupole and octopole plot, the weighting is $(5/6)^{1/2}$ and $(7/60)^{1/2}$, respectively, which accounts for 95% of the expected signal power (the remainder is in higher multipole modes; Book & Flanagan 2011). Streamlines indicate the vector field direction, and the colors indicate the vector amplitude, from violet (zero) to red (maximum).

predictions for the gravitational wave detection sensitivity of *Gaia* by the end of its mission (Section 6).

The only cosmological assumption used for the gravitational wave results is $H_\circ = 70$ km s^{-1} Mpc^{-1}. When expressed as an angular frequency, the Hubble constant becomes $H_0 = 15\ \mu$as yr^{-1}. For superluminal motion[2] calculations, we additionally assume a flat cosmology with $\Omega_M = 0.27$, and $\Omega_\Lambda = 0.73$.

2. Methods

To characterize a vector field on a sphere, one can extend the usual spherical harmonic characterization of a scalar field on a sphere to vector spherical harmonics (e.g., Thorne 1980), defined as the gradient and curl of the scalar spherical harmonics, which resemble electric (*E*) and magnetic (*B*) fields (Mignard & Klioner 2012):

$$\boldsymbol{S}_{\ell m}(\alpha, \delta) = \frac{1}{\sqrt{\ell(\ell+1)}}\ \boldsymbol{\nabla} Y_{\ell m}(\alpha, \delta), \tag{2}$$

and

$$\boldsymbol{T}_{\ell m}(\alpha, \delta) = \frac{-1}{\sqrt{\ell(\ell+1)}}\ \hat{n} \times \boldsymbol{\nabla} Y_{\ell m}(\alpha, \delta), \tag{3}$$

where the $\boldsymbol{S}_{\ell m}$ is the "spheroidal" *E*-mode of degree ℓ and order m, $\boldsymbol{T}_{\ell m}$ is the "toroidal" *B*-mode, and $\hat{n}$ is the radial unit vector. $\boldsymbol{S}_{\ell m}$, $\boldsymbol{T}_{\ell m}$, and $\hat{n}$ are mutually orthogonal, by construction. A general vector field $\boldsymbol{V}(\alpha, \delta)$ on the surface of a sphere can be expanded in terms of this vector spherical harmonic basis using complex coefficients $s_{\ell m}$ and $t_{\ell m}$:

$$\boldsymbol{V}(\alpha, \delta) = \sum_{\ell=1}^{\infty} \sum_{m=-\ell}^{\ell} (s_{\ell m} \boldsymbol{S}_{\ell m}(\alpha, \delta) + t_{\ell m} \boldsymbol{T}_{\ell m}(\alpha, \delta)). \tag{4}$$

The first three spherical harmonic degrees relevant to this treatment (*E*- and *B*-mode dipole, quadrupole, and octopole) are listed in Tables 4 and 5 and explicitly as equations with coefficients in Appendix A (but note that these equations describe a real-valued vector field and are a special case of the general complex vector spherical harmonics described by Equation (4)). We follow the Mignard & Klioner (2012) prescriptions for calculating the power in any mode (the quadrature sum of coefficients, modulo factors of 2),

$$P_\ell = s_{\ell 0}^2 + t_{\ell 0}^2 + 2 \sum_{m=1}^{\ell} ((s_{\ell m}^{Re})^2 + (s_{\ell m}^{Im})^2 + (t_{\ell m}^{Re})^2 + (t_{\ell m}^{Im})^2), \tag{5}$$

and use the *Z*-score to assess significance (Mignard & Klioner 2012, Equation (85)).

The Gwinn et al. (1997) power (sum of squared "moduli" [amplitudes]) is equivalent to the Mignard & Klioner (2012) power prescription, despite slightly different definitions. One can therefore use the quadrupole power ($\ell = 2$) as described in Equation (5) to obtain an estimate of the gravitational wave energy density:

$$\Omega_{\rm GW} = \frac{6}{5}\ \frac{1}{4\pi}\ \frac{P_2}{H_\circ^2} = 0.00042\ \frac{P_2}{(1\ \mu{\rm as\ yr}^{-1})^2}\ h_{70}^{-2}. \tag{6}$$

The factor of 6/5 in this expression corrects for the 5/6 contribution of the quadrupole to the total gravitational wave signal (Gwinn et al. 1997; Book & Flanagan 2011).

In general, a proper motion catalog that produces a limit on the quadrupole vector spherical harmonics can also provide a similar limit on the octopole (and higher orders), but the expected relative weighting on quadrupole power versus higher multipoles in a stochastic gravitational wave signal declines rapidly, as $\ell^{-4.9}$ (Book & Flanagan 2011). A quadrupole-only limit will typically be the most constraining, despite the additional information contained in higher-order modes, so a "bandpower" approach such as that used in CMB signal detection will not be effective (e.g., Bond et al. 1998). We demonstrate this explicitly using data in Section 5. Figure 1 compares an $\ell = 2$ proper motion stream plot to a $(5/6)^{1/2}\ \boldsymbol{V}_2 + (7/60)^{1/2}\ \boldsymbol{V}_3$ vector field. The quadrupole and octopole coefficients were randomly selected from normal distributions with the appropriate $\sqrt{2}$ scaling of the $m = 0$ terms. The differences between the two cases are subtle because the octopole power is de-weighted by a factor of ∼7 compared to the quadrupole.

3. Data Sources and Proper Motions

We measure proper motions from astrometric time series using VLBA data only and VLBA data combined with a single *Gaia* epoch. For both time series, we fit position versus time in R.A. and decl. separately using error-weighted linear least-squares bootstrapped to incorporate the effect of outlier epochs, as described in Truebenbach & Darling (2017).

[2] See Cohen et al. (1977), Blandford et al. (1977).

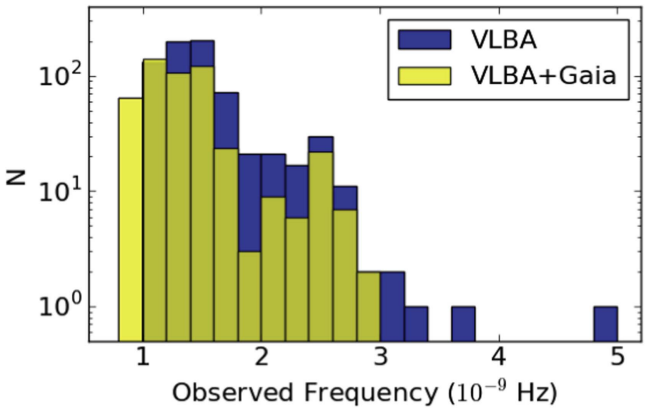

Figure 2. Distribution of observed frequencies obtained from astrometric time series of the VLBA and VLBA+*Gaia* catalogs. The upper bound on the gravitational wave frequency sensitivity of an object is the inverse of the time span used to measure its proper motion. The gravitational wave frequencies probed by these proper motions span the range 6×10^{-18} Hz $\lesssim f \lesssim 1 \times 10^{-9}$ Hz (see Section 3.1).

3.1. VLBA Catalog

The VLBA astrometric catalog is described and characterized in detail in Truebenbach & Darling (2017). In summary, the catalog contains 713 objects with mean astrometric uncertainties of 24 μas yr^{-1}. These were obtained from long-term astrometric monitoring programs as well as new observations. Proper motions were measured from astrometric time series using a bootstrapped error-weighted least-squares fit for each object in each coordinate, substantially improving on previous proper motion measurements for most objects.

The time baselines spanned by the new and archival data cover the range 6.4–27.2 years (1.2×10^{-9} Hz to 5.0×10^{-9} Hz). The median time series spans 22.2 years, which is equivalent to $f = 1.4 \times 10^{-9}$ Hz. Figure 2 shows the distribution of observed frequencies for the catalog. The majority (95%) of objects sample the range $f_{\rm obs} = (1.0\text{–}2.5) \times 10^{-9}$ Hz. The lower bound on detectable frequencies is set by the distance of the catalog objects, which must be greater than the wavelength of the gravitational waves. The sensitivity of the sample to the longest wavelength gravitational waves will therefore be a function of frequency because the sample size decreases with distance. The median redshift is 1.10, and the upper and lower quartile divisions are 0.594 and 1.64. We conservatively set the lower bound on frequency using the first redshift quartile, $z_{25\%} = 0.594$, where 75% of the sample can still be used to detect gravitational waves. Using our assumed cosmology, the light travel time is 5.74 Gyr, which corresponds to 6×10^{-18} Hz. The astrometry is therefore sensitive to gravitational waves with 6×10^{-18} Hz $\lesssim f \lesssim 1 \times 10^{-9}$ Hz.

While this catalog shows very low proper motion errors, the proper motions themselves can be substantial and significant due to relativistic radio jet motion (see Section 3.2). This "intrinsic" proper motion is uncorrelated between objects, but introduces special challenges to detecting small-amplitude correlated global proper motions. Section 4 presents a solution to this uncorrelated large-amplitude significant-signal contamination problem.

3.2. VLBA+Gaia Catalog

The first *Gaia* data release (DR1) catalog (Gaia Collaboration et al. 2016a) contains a single-epoch (2015.0) position for 2191 AGN in the International Celestial Reference Frame (ICRF2) catalog (Mignard et al. 2016). Five-hundred seventy-seven of these are VLBA sources in the Truebenbach & Darling (2017) catalog, and we use them to measure proper motions from the VLBA-*Gaia* time series. Median uncertainties in the *Gaia* astrometry of these objects are 518 μas and 459 μas in R.A. and decl., respectively.

To create a VLBA+*Gaia* proper motion catalog, we perform a 500-iteration bootstrap error-weighted least-squares fit to the VLBA time series as described by Truebenbach & Darling (2017), but we include the *Gaia* point in every fit rather than allowing it to fall into the bootstrap selection pool. This causes the *Gaia* point to act as a loose astrometric anchor, to within its uncertainty. When there are many radio epochs in a time series, the *Gaia* point will still have a minor impact on the best-fit proper motion.

We assess the *Gaia* offset from the VLBA-only proper motion prediction for the *Gaia* epoch strictly based on the uncertainty in the *Gaia* measurement, which is typically larger than the prediction uncertainty of the time series fit. The proper motions obtained from the time series that include a single *Gaia* epoch are typically not significantly altered from the VLBA-only results, but there are some notable exceptions. It is remarkable that 88% of the objects' proper motions show consistency between the radio trend and the *Gaia* position. In most of these cases (87% of the consistent subset), the measured proper motion, given its uncertainty, is consistent with zero, which implies that the optical and radio positions coincide with no motion to within the measurement uncertainty.

In 13% of the sample, the *Gaia* epoch extends the time series beyond the VLBA epochs, agrees with the VLBA proper motion, and generally improves the proper motion solution (see 0007+171 in Figure 3). We assume in these cases that the optical and radio centroids are coincident (as is the case with most objects in the sample).

In 12% of the sample, the *Gaia* epoch is significantly ($>3\sigma$) offset from the VLBA proper motion fit in one or both coordinates, indicating that the optical and radio centroids do not coincide. Figure 3 shows an example, 0003+380, where the *Gaia* astrometry is significantly offset in both coordinates. We cannot yet say whether the radio and optical proper motions differ because there is only one optical astrometric epoch. There are many possible reasons for radio-optical offsets, including optically faint jet emission, optical light from the host galaxy, dust obscuration of the AGN, and offset radio and optical emission regions within jets (e.g., Kovalev et al. 2016). Given these scenarios, it is surprising that 88% of the sample does show good radio-optical coincidence at the sub-mas level (but see Petrov & Kovalev 2017).

In 9% of the subsample with good VLBA+*Gaia* agreement (8% of the total sample), the proper motion is significant ($>5\sigma$ in at least one coordinate) and intrinsic to the object (not cosmological, caused by gravitational waves, or observer-induced). For example, 0007+171 shows a R.A. proper motion of 136.6(25.4) μas yr^{-1} (Figure 3 and Tables 6 and 7). At a redshift of $z = 1.601$ (Wills & Wills 1976), this proper motion coincides with apparent superluminal motion of 10.1(1.9)c in the object's rest frame.

Apparent velocities are calculated in the source rest frame using the proper motion distance D_M, which is equal to the line-of-sight comoving distance in a flat cosmology and related to the angular diameter distance D_A as $D_M = D_A(1 + z)$

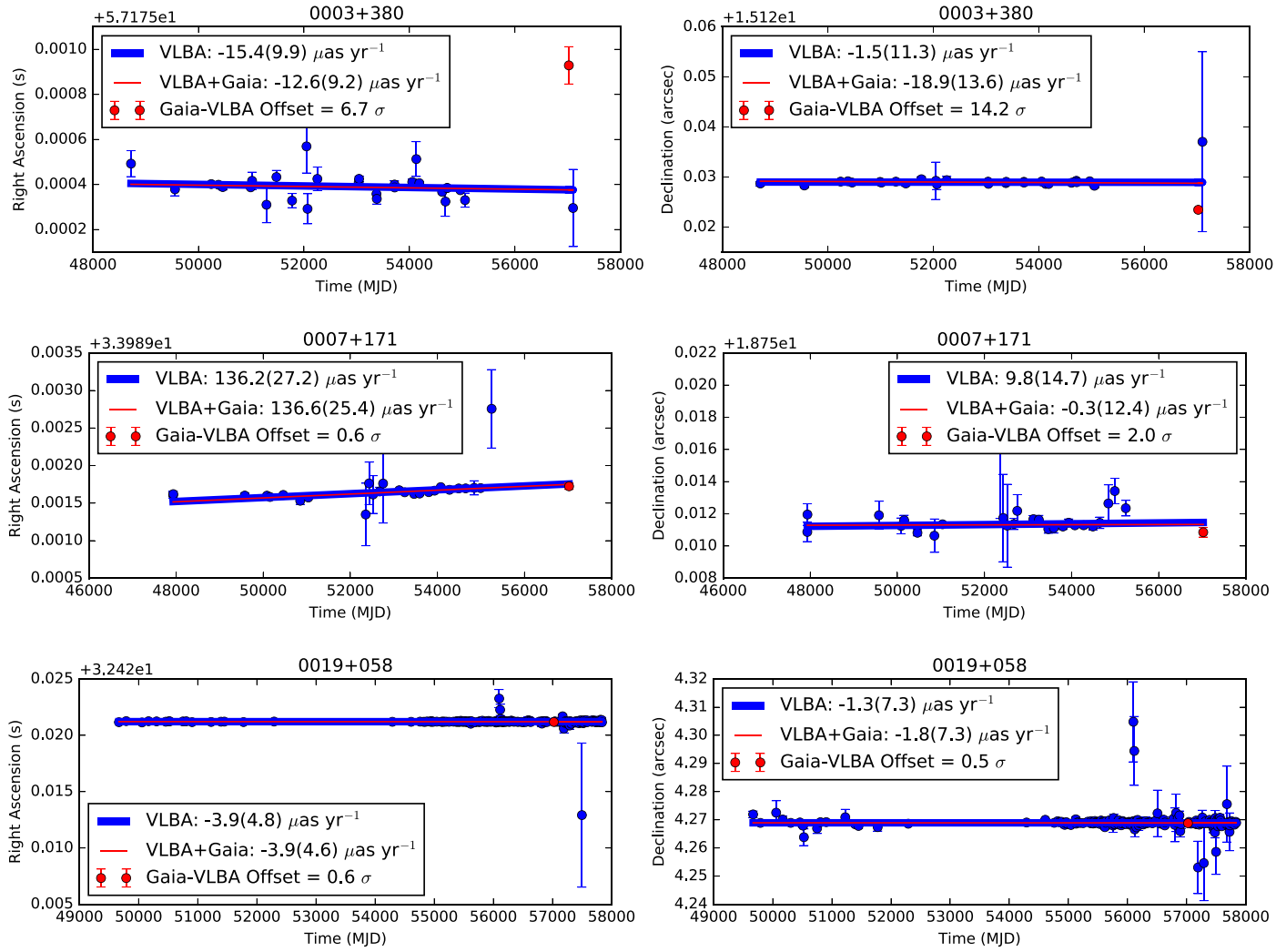

Figure 3. Example time series astrometric fits of VLBA only (blue) and VLBA plus the 2015.0 *Gaia* epoch (red). The columns depict the R.A. (left) and the decl. (right), and the proper motions and their errors are indicated in the inset boxes. Top panels: 0003+380 shows significant *Gaia*-VLBA inconsistency, indicating physical offsets between the radio and optical emission regions. Middle panels: 0007+171 shows highly significant (and superluminal) motion where the optical and radio emission regions are consistent. This is also an example of the *Gaia* epoch substantially extending the time series. Bottom panels: 0019+058 shows agreement between the VLBA and *Gaia* astrometry where no proper motion is detected. This case represents the majority (77%) of the astrometric sample.

(Hogg 1999). The redshift scale factor translates the observer-frame time interval used to calculate apparent velocity into the object rest-frame time interval. We therefore calculate the apparent transverse velocity from proper motion via

$$\boldsymbol{v} = \boldsymbol{\mu}\, D_M, \tag{7}$$

where D_M may be expressed in distance per radian or most often kpc arcsec^{-1}.

In total, there are 22 objects that show superluminal optical and radio motion, up to 10.1 c. Table 6 lists the properties of these objects. We interpret these observations to indicate that the AGN radio jets also show significant detectable optical emission, even at substantial redshifts. It is noteworthy that optical superluminal motion has only been observed in the local universe in a small number of objects including M87 and 3C264 (e.g., Biretta et al. 1999; Meyer et al. 2015).

Table 7 lists the VLBA-only and the VLBA+*Gaia* proper motions as well as the *Gaia* offsets from the VLBA-only fits. For signal extraction from this catalog, we exclude objects with significant (3σ) *Gaia* offsets in either coordinate direction. After culling, 508 objects remain in this sample, and these are used in the vector spherical harmonic fits (Sections 4 and 5).

The time baselines spanned by the VLBA+*Gaia* proper motion catalog are somewhat longer than the VLBA-only catalog (see Figure 2). Time series range from 10.6 to 37.6 years (8.4×10^{-10} Hz to 3.0×10^{-9} Hz), and the median time series spans 24.9 years, which is equivalent to $f = 1.3 \times 10^{-9}$ Hz. The majority (95%) of objects sample the range $f_{\rm obs} = 0.8$–2.5×10^{-9} Hz. The median redshift is 1.23, and the upper and lower quartile divisions are 0.73 and 1.80. The first redshift quartile, $z_{25\%} = 0.73$, with light travel time 6.55 Gyr, sets the lower bound on frequency of 5×10^{-18} Hz. The $\ell \geqslant 2$ correlated proper motions used to constrain the stochastic gravitational wave background are therefore sensitive to waves with frequencies 5×10^{-18} Hz $\lesssim f \lesssim 0.8 \times 10^{-9}$ Hz.

3.3. Gaia Catalog

The advantages of extragalactic *Gaia* proper motions over radio interferometric proper motions lie in the factor of ∼1000 increase in number of optical sources over radio and the

(generally) lower intrinsic optical proper motions. These advantages may overcome the less precise astrometry and shorter time baseline of *Gaia* compared to geodetic VLBI monitoring (in the short term).

The *Gaia* DR1 catalog contains a single-epoch position for AGN, but the expected end-of-mission proper motion uncertainties can be used to predict the sensitivity of the final *Gaia* catalog to gravitational waves. To first order, the vector proper motion error of each object depends on its ecliptic angle and optical *G*-band magnitude.[3] We use the `pyGaia`[4] package to predict the proper motion errors for each object in the 567,721 AGN Paine et al. (2018) *WISE-Gaia* sample. Paine et al. (2018) present the expected uncertainties, the sky distribution, and the potential systematics of the sample. We use this catalog in Section 6 to predict the expected *Gaia* end-of-mission sensitivity to the stochastic gravitational wave background.

4. Signal Extraction

The challenge to vector spherical harmonic fitting posed by radio sources is their often significant large apparent intrinsic proper motions induced by relativistic jets. These intrinsic proper motions are uncorrelated between objects but can dominate an error-weighted least-squares fit of the correlated proper motions. Investigators measuring the secular aberration drift dipole have therefore heavily censored their samples in order to maximize the signal of interest (e.g., Titov et al. 2011; Titov & Lambert 2013), but this requires a priori knowledge of the expected signal. A different approach can be bootstrap resampling, which was successfully implemented by Truebenbach & Darling (2017) to extract the secular aberration drift dipole induced by the barycenter acceleration about the Galactic Center with minimal data clipping.

Here, we implement a maximum likelihood MCMC "permissive fit" method that allows for highly significant large-departure data points by assuming that the mismatch between model and data will in some cases be bounded from below by the measured uncertainty (Sivia & Skilling 2006, p. 168). This method, rather than minimizing an error-weighted data-model residual $R_i = (D_i - \text{Model})/\sigma_i$ for each data point D_i with uncertainty σ_i, maximizes the logarithm of the posterior probability density function

$$L = \text{constant} + \sum_{i=1}^{N} \ln\left(\frac{1 - e^{-R_i^2/2}}{R_i^2}\right). \quad (8)$$

In this work, the data are the positions and proper motions of extragalactic objects, the model is a linear combination of vector spherical harmonics evaluated at each object position, and the uncertainties are the proper motion errors (uncertainties in the positions of objects have no impact on low-ℓ signals). To assess the model fits and uncertainties, we employ an MCMC technique using `lmfit` (Newville et al. 2014) to obtain the maximum likelihood and confidence intervals for each fit parameter directly from the resulting distribution of outcomes.

For the vector spherical harmonic fits, all coefficients and uncertainties are maximum likelihood estimates. The power in a given mode is calculated from Equation (5), and its significance is estimated using a *Z*-score following Mignard & Klioner (2012), Equation (85).

[3] https://www.cosmos.esa.int/web/gaia/science-performance
[4] https://pypi.python.org/pypi/PyGaia

Table 1
Dipole Fits

	VLBA	VLBA+*Gaia*
Quantity	Amplitude (μas yr^{-1})	Amplitude (μas yr^{-1})
E-mode Dipole (Aberration Drift)		
s_{10}	−2.24(0.74)	−1.52(0.78)
s_{11}^{Re}	−0.50(0.53)	−0.21(0.53)
s_{11}^{Im}	−3.07(0.54)	−3.29(0.61)
$\sqrt{P_1^s}$	**4.93(0.76)**	**4.91(0.85)**
Z-score[a]	5.5	5.1
B-mode Dipole (Rotation)		
t_{10}	−0.72(0.62)	−0.51(0.68)
t_{11}^{Re}	+1.17(0.52)	0.76(0.55)
t_{11}^{Im}	−0.40(0.66)	−0.36(0.68)
$\sqrt{P_1^t}$	**1.89(0.74)**	**1.29(0.79)**
Z-score[a]	1.2	0.1

Notes. Fits are simultaneously made to electric and magnetic dipole vector fields.
[a] This statistic is unitless.

4.1. The Secular Aberration Drift Dipole

We start with a fit of the *E*- and *B*-mode dipole signals in both catalogs, which must be removed from vector fields before attempting to measure higher-order modes. While the vector spherical harmonics are orthonormal in principle, there can be correlation between degrees and orders when fitting the harmonics to discrete sparsely sampled nonuniform noisy data, so "nuisance" signals must be subtracted. We simultaneously fit for both *E*- and *B*-mode dipoles (aberration drift and rotation, respectively) to capture any residual signature of a non-inertial frame (or other cosmic rotation) as well as any correlations between the two modes (even if the *B*-mode dipole is nonsignificant, there can still be crosstalk with the *E*-mode dipole). Following Mignard & Klioner (2012), the dipole equations are listed in Tables 4 and 5 and explicitly as equations with coefficients in Appendix A.

Table 1 lists the dipole fit coefficients for the VLBA and VLBA+*Gaia* samples. We significantly detect the secular aberration drift with 5.5σ and 5.1σ significance, respectively. The *E*-mode dipole apex lies at 279.°2(9.°8), −27.°0(8.°7) and 274.°0(9.°3), −18.°0(9.°2) and is consistent with the Galactic Center (266.°4, −29.°0) in each case (Figure 4). The dipole amplitude is 1.70(0.26) and 1.70(0.29) μas yr^{-1}, which is substantially smaller than expected. For example, Titov & Lambert (2013) find 6.4(1.1) μas yr^{-1}, and Xu et al. (2013) obtain 5.8(0.3) μas yr^{-1}. These are consistent with the expectation of 5.5(0.2) μas yr^{-1} based on barycenter orbital parameters obtained from Galactic maser parallaxes and proper motions and the Sgr A* reflex motion (Reid et al. 2014). The amplitude of the dipole measured here is likely suppressed by the no-net-rotation constraint imposed by the global fitting used to produce the ICRF catalog (see Truebenbach & Darling (2017) for a detailed discussion). For the purposes of detecting higher multipole modes in the proper motion data, we simply need to measure whatever dipole is present and subtract the dipole fit from each proper motion catalog before fitting higher multipoles to extract (or constrain) the gravitational wave signal.

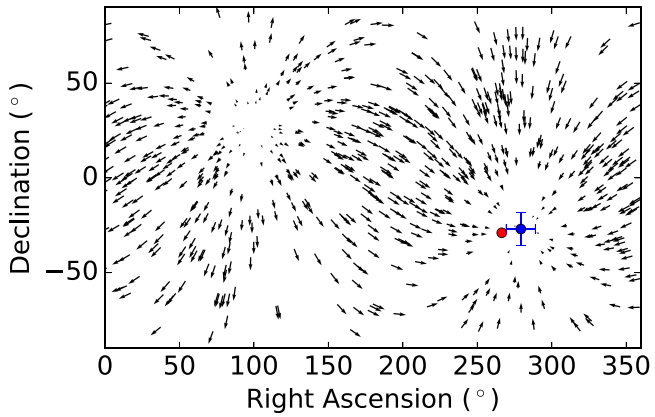

Figure 4. Maximum likelihood secular aberration drift (*E*-mode dipole) model fit to the VLBA sample plotted in equatorial coordinates. The fit parameters and uncertainties are listed in Table 1. The red circle indicates the Galactic Center, and the point with the error bars shows the dipole apex obtained from the dipole (simultaneous *E*- and *B*-mode) fit.

No rotation is detected: the *B*-mode dipole fits are not significant (1.2σ or less), with square root power of 1.89(0.74) μas yr^{-1} for the VLBA catalog and 1.29(0.79) μas yr^{-1} for VLBA+*Gaia*. These correspond to angular rotation rates of 0.65(0.26) and 0.45(0.27) μas yr^{-1}, respectively.

4.2. Constraints on Gravitational Waves

For each catalog, we simultaneously fit *E*- and *B*-mode quadrupolar vector spherical harmonics for the best constraint on the stochastic gravitational wave background. We also simultaneously fit *E*- and *B*-mode quadrupole and octopole coefficients, but this fit is less constraining than quadrupole alone, as described in Section 2 and demonstrated explicitly in Section 5. Measuring the quadrupole and octopole powers separately is a way to test the isotropy of the background, which is assumed when combining the two modes to obtain a limit on $\Omega_{\rm GW}$. The quadrupole and octopole vector spherical harmonics are listed in Tables 4 and 5 and explicitly as equations with coefficients in Appendix A, Equations (11)–(14).

It is incorrect to obtain a limit on $\Omega_{\rm GW}$ from the parameters of a nonsignificant quadrupole fit to a vector field. When no significant signal is detected, we follow the method described by Gwinn et al. (1997): assuming independent Gaussian errors on the fit coefficients as determined using the above methods, we resample the fit components and recalculate the quadrupole power 10000 times. We set the upper limit to be 95th percentile of the quadrupole power distribution. This method gives a less-constraining result than has been quoted in previous work, such as Titov et al. (2011).

A stochastic gravitational wave background (or a reliable limit) should show equal power in the *E*- and *B*-modes (Book & Flanagan 2011). One can therefore identify spurious, nongravitational wave signals by comparing the power in the two modes.

5. Results

5.1. VLBA

We fit the vector spherical harmonic quadrupole to the Truebenbach & Darling (2017) VLBA proper motion catalog with minimal restrictions on the fit sample. We omit two objects with proper motion amplitudes greater than 1 milliarcsec yr^{-1}, leaving 711 objects in the catalog. After *E*-mode dipole subtraction, a simultaneous *E*- and *B*-mode quadrupole fit produced no significant signal, with a total quadrupole power of $\sqrt{P_2} = 1.83(0.72)$ μas yr^{-1}. Table 2 shows the fit components, mutually consistent (and nonsignificant) *E*- and *B*-mode powers ($\sqrt{P_2^s} = 1.46(0.69)$ μas yr^{-1} and $\sqrt{P_2^t} = 1.11(0.77)$ μas yr^{-1}, respectively), and the *Z*-score of the fit. Using the resampling method described above (Section 4.2), we obtain a 95% confidence limit on the stochastic gravitational wave energy density of $\Omega_{\rm GW} < 0.0064$ (see Equation (6)). Direct conversion of the nonsignificant quadrupolar power to energy density gives a smaller (nonsignificant) value: $\Omega_{\rm GW} = 0.0014(0.0011)$. This is roughly equivalent to a dimensionless gravitational wave strain amplitude of $h \simeq 10^{-10}$ for $f \simeq 10^{-9}$ Hz ($h \sim (H_0/f)\sqrt{\Omega_{\rm GW}}$; Book & Flanagan 2011). The maximum proper motion amplitude in the quadrupole is 1.0 μas yr^{-1}, which is equivalent to $h \simeq 10^{-10}$ for $f \simeq 10^{-9}$ Hz ($h \sim \mu/f$).

A simultaneous quadrupole and octopole fit in both *E*- and *B*-modes produces a weaker constraint on the stochastic gravitational wave background, as expected (see Section 2): $\sqrt{P_2} = 3.53(1.09)$ μas yr^{-1}, $\sqrt{P_3} = 4.98(0.92)$ μas yr^{-1}, and $\Omega_{\rm GW} < 0.032$ (95% confidence limit). To calculate the above limit on $\Omega_{\rm GW}$ from the nonsignificant quadrupole and octopole fits, we substitute a weighted power into Equation (6), $1.05(P_2 + P_3)$ in the place of $(6/5)P_2$, and resample the fit coefficients to find a 95% confidence limit. Table 3 lists the coefficients, mode powers, and *Z*-scores for this fit.

Table 2
Quadrupole Fits

Quantity	VLBA Amplitude (μas yr^{-1})	VLBA+*Gaia* Amplitude (μas yr^{-1})
Quadrupole		
s_{20}	0.83(0.72)	1.72(0.78)
s_{21}^{Re}	0.80(0.47)	1.16(0.52)
s_{21}^{Im}	−0.22(0.48)	−0.49(0.51)
s_{22}^{Re}	−0.17(0.58)	−0.04(0.59)
s_{22}^{Im}	0.06(0.44)	0.74(0.46)
$\sqrt{P_2^s}$	**1.46(0.69)**	**2.70(0.74)**
t_{20}	−0.48(0.66)	−1.17(0.70)
t_{21}^{Re}	0.01(0.50)	−0.68(0.58)
t_{21}^{Im}	−0.16(0.43)	−0.41(0.47)
t_{22}^{Re}	0.43(0.53)	0.25(0.56)
t_{22}^{Im}	0.54(0.60)	0.81(0.60)
$\sqrt{P_2^t}$	**1.11(0.77)**	**2.01(0.78)**
$\sqrt{P_2}$	**1.83(0.72)**	**3.36(0.75)**
Z-score[a]	−0.7	1.9

Notes. Fits are simultaneously made to electric and magnetic quadrupole vector fields. Parenthetical quantities indicate 1σ uncertainties.
[a] This statistic is unitless.

5.2. VLBA+Gaia

We subtract the *E*-mode dipole and then fit the vector spherical harmonic quadrupole to the 508-object VLBA+*Gaia* proper motion catalog with no proper motion restrictions. The simultaneous *E*- and *B*-mode quadrupole fit is not significant; the total quadrupole power is $\sqrt{P_2} = 3.36(0.75)$ μas yr^{-1}, and the *E*- and *B*-mode powers are consistent: $\sqrt{P_2^s} = 2.70(0.74)$ μas yr^{-1} and $\sqrt{P_2^t} = 2.01(0.78)$ μas yr^{-1}, respectively. Table 2 lists the fit

Table 3
Quadrupole and Octopole Fits

Quantity	VLBA Amplitude (μas yr^{-1})	VLBA+*Gaia* Amplitude (μas yr^{-1})
Quadrupole		
s_{20}	0.55(0.98)	0.58(0.70)
s_{21}^{Re}	0.88(0.62)	0.29(0.71)
s_{21}^{Im}	−0.30(0.52)	−0.99(0.61)
s_{22}^{Re}	−0.28(0.69)	−0.42(0.76)
s_{22}^{Im}	0.04(0.30)	0.05(0.54)
t_{20}	−0.27(0.20)	−0.18(0.53)
t_{21}^{Re}	0.78(0.63)	−0.10(0.57)
t_{21}^{Im}	0.13(0.36)	−1.01(0.48)
t_{22}^{Re}	−0.50(0.37)	0.02(0.01)
t_{22}^{Im}	2.05(0.84)	1.66(0.83)
$\sqrt{P_2}$	**3.53(1.09)**	**3.23(1.01)**
Z-score[a]	1.9	1.2
Octopole		
s_{30}	−0.75(0.87)	−0.34(1.02)
s_{31}^{Re}	−0.35(0.18)	0.42(0.53)
s_{31}^{Im}	0.00(0.24)	0.82(0.73)
s_{32}^{Re}	1.57(0.66)	1.10(0.66)
s_{32}^{Im}	0.59(0.61)	0.61(0.51)
s_{33}^{Re}	0.60(0.53)	−0.37(0.52)
s_{33}^{Im}	0.85(0.58)	0.39(0.58)
t_{30}	−0.10(0.81)	−0.41(0.96)
t_{31}^{Re}	−1.43(0.58)	−2.68(0.62)
t_{31}^{Im}	0.78(0.53)	0.94(0.57)
t_{32}^{Re}	0.90(0.59)	0.86(0.60)
t_{32}^{Im}	−0.77(0.49)	−0.04(0.73)
t_{33}^{Re}	−2.01(0.75)	−0.73(0.84)
t_{33}^{Im}	−0.12(0.61)	−0.90(0.57)
$\sqrt{P_3}$	**4.98(0.92)**	**5.10(0.89)**
Z- score[a]	3.4	2.6

Notes. Fits are simultaneously made to electric and magnetic quadrupole and octopole vector fields. Parenthetical quantities indicate 1σ uncertainties.
[a] This statistic is unitless.

components and the *Z*-score of the fit. The 95% confidence limit on the stochastic gravitational wave energy density is $\Omega_{\rm GW} < 0.011$ (see Equation (6)).

The simultaneous quadrupole and octopole fit in both *E*- and *B*-modes yields $\sqrt{P_2} = 3.23(1.01)$ μas yr^{-1}, $\sqrt{P_3} = 5.10(0.89)$ μas yr^{-1}, and $\Omega_{\rm GW} < 0.028$ (95% confidence limit). This limit on the stochastic gravitational wave background is less constraining than the quadrupole-only fit, as expected, but is slightly more constraining than the VLBA-only quadrupole plus octopole fit. Table 3 lists the coefficients, mode powers, and *Z*-scores for this fit.

6. *Gaia* Predictions

The rough expectation for a stochastic gravitational wave background limit obtained from *Gaia* presented by Book & Flanagan (2011) was $\Omega_{\rm GW} \lesssim 10^{-6}$ for $f \lesssim 10^{-8}$ Hz, but this was under the assumption of a proper motion uncertainty of $\sigma_\mu = 10$ μas yr^{-1} per source and using 10^6 objects. The revised end-of-mission error budgets, which have the largest impact on faint sources, have $\sigma_\mu \sim 200$ μas yr^{-1} per quasar, and $\sim 5 \times 10^5$ objects (Paine et al. 2018), so we expect $\Omega_{\rm GW} \lesssim 10^{-3}$.

To confirm this expectation, we use the expected end-of-mission proper motion errors on the extragalactic *Gaia-WISE* catalog compiled by Paine et al. (2018) and described in Section 3.3. We randomly sample vector proper motions from within the predicted error budget for each object assuming Gaussian errors. Provided that the barycenter acceleration about the Galactic Center can be removed from the data, the resulting proper motions should be uncorrelated and represent a no-signal noisy data set that can be used to predict the best possible limit on a gravitational wave signal. Unlike the *Gaia* Universe model snapshot (GUMS) sample (Robin et al. 2012), this catalog represents real objects detected in *Gaia* that will likely be employed when final proper motions are measured.

After randomly sampling from within the proper motion error budgets for each object, we performed an error-weighted least-squares fit of 500 randomly generated *E*- and *B*-mode quadrupolar gravitational wave signals with the quadrupolar power in the range $0.5\ \mu{\rm as\ yr}^{-1} \leqslant \sqrt{P_2} \leqslant 5\ \mu{\rm as\ yr}^{-1}$ in 25 logarithmic steps with 20 trials each. For each trial, we add the input proper motion quadrupolar signal to the catalog proper motions and then fit simultaneous *E*- and *B*-mode quadrupole vector spherical harmonics (listed in Appendix A) to obtain a fit power. For each input power, we calculate the mean and standard deviation of the best-fit power to assess the offset and scatter of the fit compared to the input.

Figure 5 shows the results of these fit trials, recast in terms of $\Omega_{\rm GW}$. For $\Omega_{\rm GW} \gtrsim 10^{-3}$, we reliably recover the input gravitational wave signal with some scatter, but a clear noise floor arises for $\Omega_{\rm GW} \lesssim 6 \times 10^{-4}$ such that the (nonsignificant) fit does not fall below $\Omega_{\rm GW} \sim 6 \times 10^{-4}$. This is the limit on the stochastic gravitational wave background that *Gaia* may achieve using the Paine et al. (2018) *Gaia-WISE* extragalactic proper motion catalog, which agrees with the rough expectation above.

7. Discussion

The VLBA+*Gaia* fits are less constraining on the stochastic gravitational wave background than the VLBA-only fits, despite the generally improved proper motion solutions obtained from the VLBA+*Gaia* time series. Because $\Omega_{\rm GW}$ depends on the vector spherical harmonic mode power, it will scale roughly as N, not $\sqrt{N}$, and the reduced VLBA+*Gaia* sample size should decrease sensitivity by a factor of roughly $\sqrt{2}$ compared to the VLBA-only sample. The sample size accounts for some, but not all, of the difference in limits on $\Omega_{\rm GW}$.

The expected *Gaia* proper motions, despite the substantially lower precision compared to radio-based astrometry, will further constrain the stochastic gravitational wave background by roughly an order of magnitude due to the larger extragalactic sample size available in visible light. The *Gaia* proper motions are also expected to be less dominated by the intrinsic proper motions caused by relativistic AGN jets. While the VLBA+*Gaia* sample identified 22 new cases of radio and optical superluminal motion and 23 cases of subluminal significant intrinsic proper motion (8% of the 577-object sample in total), these are radio-selected objects. The Paine et al. (2018) *Gaia-WISE* sample is optical- and infrared-selected and will therefore not be so

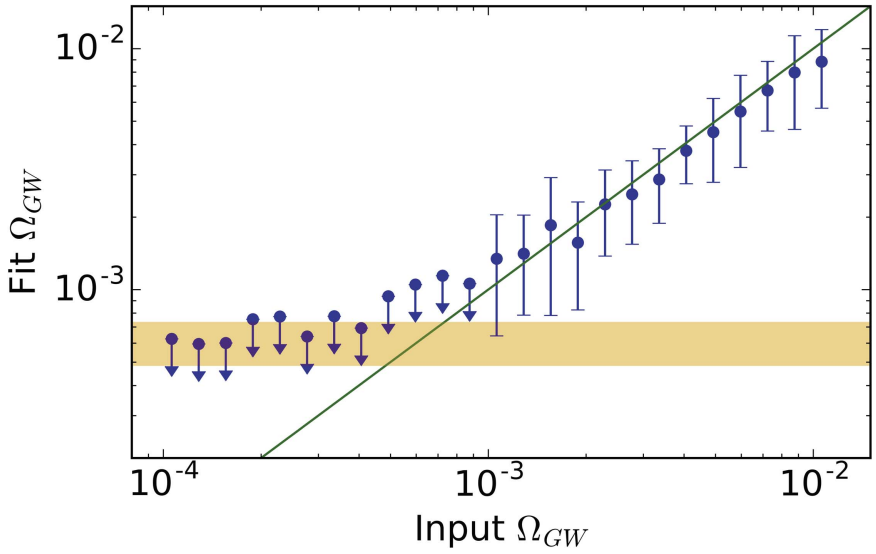

Figure 5. Fit vs. input values for the stochastic gravitational wave background energy density, $\Omega_{\rm GW}$, expected from *Gaia* proper motions. Points and their error bars indicate the mean and standard deviation of 20 recovery trials per random injected signal. Arrows indicate nonsignificant fits. The green line indicates the one-to-one perfect signal recovery locus, and the orange bar shows the $\Omega_{\rm GW} = 6 \times 10^{-4}$ noise floor imposed by the end-of-mission *Gaia* proper motion sensitivity to AGN in the *Gaia-WISE* catalog.

jet-dominated as a VLBI radio-selected sample, and it is therefore reasonable to assume that the vast majority of *Gaia* objects will show no detectable intrinsic proper motion.

The astrometric gravitational wave limit may be improved by increasing the sample size in either radio or visible light. Identifying additional AGN in the *Gaia* catalog may decrease the expected $\Omega_{\rm GW}$ noise floor by at most a factor of 2 if one can achieve a 10^6-object sample. In this case, one might achieve $\Omega_{\rm GW} \lesssim 2 \times 10^{-4}$, which is nonetheless substantially larger than the $\sim 10^{-6}$ value predicted by Book & Flanagan (2011). Improvements could also arise from an extended *Gaia* mission or better-than-expected performance of the main mission. Enhancing the radio sample size is a possibility, perhaps by an order of magnitude. Assuming similar astrometric precision and intrinsic proper motions to the current catalog, this would reduce the 95% confidence limit to $\Omega_{\rm GW} \lesssim 6 \times 10^{-4}$, which is similar to the *Gaia* limit.

8. Conclusions

We have obtained limits on the low-frequency stochastic gravitational wave background using VLBA astrometry alone and VLBA astrometry combined with the first *Gaia* epoch. We demonstrate that a quadrupole signal is the most constraining and obtain 95% confidence limits on the gravitational wave energy density of $\Omega_{\rm GW} < 0.0064$ over the frequency range $6 \times 10^{-18}\,{\rm Hz} \lesssim f \lesssim 1 \times 10^{-9}\,{\rm Hz}$ for the VLBA proper motions. When *Gaia* is included, proper motion errors improve, but the limit is less constraining mainly due to a reduced sample size: $\Omega_{\rm GW} < 0.011$. The noise threshold for the VLBA fit is roughly equivalent to a dimensionless gravitational wave strain amplitude of $h \simeq 10^{-10}$ for $f \simeq 10^{-9}\,{\rm Hz}$.

We also predict the limit that may be obtained with the full *Gaia* data release that includes proper motions (or limits) of AGN. One hurtle is the identification of AGN among the 1000-fold more numerous stars in the *Gaia* catalog and finding an all-sky distribution that is amenable to low-ℓ mode fitting, but provided this can be done (see Paine et al. 2018), then we predict that *Gaia* will find a noise floor of $\Omega_{\rm GW} \lesssim 6 \times 10^{-4}$ using $\sim 6 \times 10^5$ objects.

Astrometric limits on the stochastic gravitational wave background will continue to improve with time as geodetic monitoring of radio-loud AGN continues, but substantial improvements will need to come from growing the number of objects monitored. The next post-*Gaia* advance could be made by a Next Generation Very Large Array were it to have substantial collecting area on VLBA baselines (Bower et al. 2015).

We thank David Gordon (NASA Goddard Space Flight Center) for making much of this work possible and Mark Reid (Smithsonian Astrophysical Observatory) for helpful discussions. We also thank the anonymous referee for helpful suggestions. The authors acknowledge support from the NSF grant AST-1411605 and the NASA grant 14-ATP14-0086. This work has made use of data from the European Space Agency (ESA) mission *Gaia* (https://www.cosmos.esa.int/gaia), processed by the *Gaia* Data Processing and Analysis Consortium (DPAC, https://www.cosmos.esa.int/web/gaia/dpac/consortium). Funding for the DPAC has been provided by national institutions, in particular the institutions participating in the *Gaia* Multilateral Agreement. We acknowledge the *Gaia* Project Scientist Support Team and the *Gaia* Data Processing and Analysis Consortium for the `pyGaia` software. This research has made use of NASA's Astrophysics Data System Bibliographic Services and the NASA/IPAC Extragalactic Database (NED), which is operated by the Jet Propulsion Laboratory, California Institute of Technology, under contract with the National Aeronautics and Space Administration.

Facilities: *Gaia*, VLBA.

Software: lmfit (Newville et al. 2014), pyGaia.

Appendix A
Vector Spherical Harmonics

Here, we present explicit formulae for the $\ell \leqslant 3$ vector spherical harmonics based on those described in Mignard & Klioner (2012) for real-valued vector fields but that have strictly real coefficients (and therefore have sign differences) and explicitly include factors of 2 that are needed for correct power calculations.

The vector spherical harmonics for the electric and magnetic dipoles described by Mignard & Klioner (2012) and listed in Tables 4 and 5 are

$$\begin{aligned}\boldsymbol{V}_{E1}(\alpha,\,\delta) = &\left(s_{11}^{Re}\,\frac{1}{2}\sqrt{\frac{3}{\pi}}\,\sin\alpha + s_{11}^{Im}\,\frac{1}{2}\sqrt{\frac{3}{\pi}}\,\cos\alpha\right)\hat{\boldsymbol{e}}_{\alpha}\\ &+\left(s_{10}\,\frac{1}{2}\sqrt{\frac{3}{2\pi}}\,\cos\delta + s_{11}^{Re}\,\frac{1}{2}\sqrt{\frac{3}{\pi}}\,\cos\alpha\sin\delta\right.\\ &\left.-\,s_{11}^{Im}\,\frac{1}{2}\sqrt{\frac{3}{\pi}}\,\sin\alpha\sin\delta\right)\hat{\boldsymbol{e}}_{\delta}\end{aligned} \tag{9}$$

and

$$\begin{aligned}\boldsymbol{V}_{M1}(\alpha,\,\delta) = &\left(t_{10}\,\frac{1}{2}\sqrt{\frac{3}{2\pi}}\,\cos\delta + t_{11}^{Re}\,\frac{1}{2}\sqrt{\frac{3}{\pi}}\,\cos\alpha\sin\delta\right.\\ &\left.-\,t_{11}^{Im}\,\frac{1}{2}\sqrt{\frac{3}{\pi}}\,\sin\alpha\sin\delta\right)\hat{\boldsymbol{e}}_{\alpha}\\ &+\left(-t_{11}^{Re}\,\frac{1}{2}\sqrt{\frac{3}{\pi}}\,\sin\alpha - t_{11}^{Im}\,\frac{1}{2}\sqrt{\frac{3}{\pi}}\,\cos\alpha\right)\hat{\boldsymbol{e}}_{\delta},\end{aligned} \tag{10}$$

where the $s_{\ell m}$ are the amplitudes of the spheroidal (curl-free or *E*-mode) orders, the $t_{\ell m}$ are the amplitudes of the toroidal (divergence-less or *B*-mode) orders, and $\hat{\boldsymbol{e}}_{\alpha}$ and $\hat{\boldsymbol{e}}_{\delta}$ are the unit vectors in the R.A. and decl. directions, respectively.

The quadrupole vector spherical harmonics are

$$\begin{aligned}\boldsymbol{V}_{E2}(\alpha,\,\delta) = &\left(s_{21}^{Re}\,\frac{1}{2}\sqrt{\frac{5}{\pi}}\,\sin\alpha\sin\delta + s_{21}^{Im}\,\frac{1}{2}\sqrt{\frac{5}{\pi}}\,\cos\alpha\sin\delta\right.\\ &\left.-s_{22}^{Re}\,\frac{1}{2}\sqrt{\frac{5}{\pi}}\,\sin 2\alpha\cos\delta - s_{22}^{Im}\,\frac{1}{2}\sqrt{\frac{5}{\pi}}\,\cos 2\alpha\cos\delta\right)\hat{\boldsymbol{e}}_{\alpha}\\ &+\left(s_{20}\,\frac{1}{4}\sqrt{\frac{15}{2\pi}}\,\sin 2\delta - s_{21}^{Re}\,\frac{1}{2}\sqrt{\frac{5}{\pi}}\,\cos\alpha\cos 2\delta\right.\\ &+s_{21}^{Im}\,\frac{1}{2}\sqrt{\frac{5}{\pi}}\,\sin\alpha\cos 2\delta - s_{22}^{Re}\,\frac{1}{4}\sqrt{\frac{5}{\pi}}\,\cos 2\alpha\sin 2\delta\\ &\left.+s_{22}^{Im}\,\frac{1}{4}\sqrt{\frac{5}{\pi}}\,\sin 2\alpha\sin 2\delta\right)\hat{\boldsymbol{e}}_{\delta}\end{aligned} \tag{11}$$

Table 4
Spheroidal (*E*-mode) Vector Spherical Harmonics ($\ell \leqslant 3$)

ℓ, m	Amplitude	$\hat{\boldsymbol{e}}_{\alpha}$	$\hat{\boldsymbol{e}}_{\delta}$
1,0	$\frac{1}{2}\sqrt{\frac{3}{2\pi}}$	0	$\cos\delta$
1,1 (Re)	$\frac{1}{2}\sqrt{\frac{3}{\pi}}$	$\sin\alpha$	$\cos\alpha\sin\delta$
1,1 (Im)	$\frac{1}{2}\sqrt{\frac{3}{\pi}}$	$\cos\alpha$	$-\sin\alpha\sin\delta$
2,0	$\frac{1}{4}\sqrt{\frac{15}{2\pi}}$	0	$\sin 2\delta$
2,1 (Re)	$\frac{1}{2}\sqrt{\frac{5}{\pi}}$	$\sin\alpha\sin\delta$	$-\cos\alpha\cos 2\delta$
2,1 (Im)	$\frac{1}{2}\sqrt{\frac{5}{\pi}}$	$\cos\alpha\sin\delta$	$\sin\alpha\cos 2\delta$
2,2 (Re)	$\frac{1}{4}\sqrt{\frac{5}{\pi}}$	$-2\sin 2\alpha\cos\delta$	$-\cos 2\alpha\sin 2\delta$
2,2 (Im)	$\frac{1}{4}\sqrt{\frac{5}{\pi}}$	$-2\cos 2\alpha\cos\delta$	$\sin 2\alpha\sin 2\delta$
3,0	$\frac{1}{8}\sqrt{\frac{21}{\pi}}$	0	$(5\sin^2\delta - 1)\cos\delta$
3,1 (Re)	$\frac{1}{8}\sqrt{\frac{7}{\pi}}$	$\sin\alpha(5\sin^2\delta - 1)$	$\cos\alpha\sin\delta(15\sin^2\delta - 11)$
3,1 (Im)	$\frac{1}{8}\sqrt{\frac{7}{\pi}}$	$\cos\alpha(5\sin^2\delta - 1)$	$-\sin\alpha\sin\delta(15\sin^2\delta - 11)$
3,2 (Re)	$\frac{1}{4}\sqrt{\frac{35}{2\pi}}$	$-\sin 2\alpha\sin 2\delta$	$-\cos 2\alpha\cos\delta(3\sin^2\delta - 1)$
3,2 (Im)	$\frac{1}{4}\sqrt{\frac{35}{2\pi}}$	$-\cos 2\alpha\sin 2\delta$	$\sin 2\alpha\cos\delta(3\sin^2\delta - 1)$
3,3 (Re)	$\frac{1}{8}\sqrt{\frac{105}{\pi}}$	$\sin 3\alpha\cos^2\delta$	$\cos 3\alpha\cos^2\delta\sin\delta$
3,3 (Im)	$\frac{1}{8}\sqrt{\frac{105}{\pi}}$	$\cos 3\alpha\cos^2\delta$	$-\sin 3\alpha\cos^2\delta\sin\delta$

Table 5
Toroidal (*B*-mode) Vector Spherical Harmonics ($\ell \leqslant 3$)

ℓ, m	Amplitude	$\hat{\boldsymbol{e}}_{\alpha}$	$\hat{\boldsymbol{e}}_{\delta}$
1,0	$\frac{1}{2}\sqrt{\frac{3}{2\pi}}$	$\cos\delta$	0
1,1 (Re)	$\frac{1}{2}\sqrt{\frac{3}{\pi}}$	$\cos\alpha\sin\delta$	$-\sin\alpha$
1,1 (Im)	$\frac{1}{2}\sqrt{\frac{3}{\pi}}$	$-\sin\alpha\sin\delta$	$-\cos\alpha$
2,0	$\frac{1}{4}\sqrt{\frac{15}{2\pi}}$	$\sin 2\delta$	0
2,1 (Re)	$\frac{1}{2}\sqrt{\frac{5}{\pi}}$	$-\cos\alpha\cos 2\delta$	$-\sin\alpha\sin\delta$
2,1 (Im)	$\frac{1}{2}\sqrt{\frac{5}{\pi}}$	$\sin\alpha\cos 2\delta$	$-\cos\alpha\sin\delta$
2,2 (Re)	$\frac{1}{4}\sqrt{\frac{5}{\pi}}$	$-\cos 2\alpha\sin 2\delta$	$2\sin 2\alpha\cos\delta$
2,2 (Im)	$\frac{1}{4}\sqrt{\frac{5}{\pi}}$	$\sin 2\alpha\sin 2\delta$	$2\cos 2\alpha\cos\delta$
3,0	$\frac{1}{8}\sqrt{\frac{21}{\pi}}$	$(5\sin^2\delta - 1)\cos\delta$	0
3,1 (Re)	$\frac{1}{8}\sqrt{\frac{7}{\pi}}$	$\cos\alpha\sin\delta(15\sin^2\delta - 11)$	$-\sin\alpha(5\sin^2\delta - 1)$
3,1 (Im)	$\frac{1}{8}\sqrt{\frac{7}{\pi}}$	$-\sin\alpha\sin\delta(15\sin^2\delta - 11)$	$-\cos\alpha(5\sin^2\delta - 1)$
3,2 (Re)	$\frac{1}{4}\sqrt{\frac{35}{2\pi}}$	$-\cos 2\alpha\cos\delta(3\sin^2\delta - 1)$	$\sin 2\alpha\sin 2\delta$
3,2 (Im)	$\frac{1}{4}\sqrt{\frac{35}{2\pi}}$	$\sin 2\alpha\cos\delta(3\sin^2\delta - 1)$	$\cos 2\alpha\sin 2\delta$
3,3 (Re)	$\frac{1}{8}\sqrt{\frac{105}{\pi}}$	$\cos 3\alpha\cos^2\delta\sin\delta$	$-\sin 3\alpha\cos^2\delta$
3,3 (Im)	$\frac{1}{8}\sqrt{\frac{105}{\pi}}$	$-\sin 3\alpha\cos^2\delta\sin\delta$	$-\cos 3\alpha\cos^2\delta$

and

$$\begin{aligned}\boldsymbol{V}_{M2}(\alpha,\,\delta) = &\left(t_{20}\,\frac{1}{4}\sqrt{\frac{15}{2\pi}}\,\sin 2\delta - t_{21}^{Re}\,\frac{1}{2}\sqrt{\frac{5}{\pi}}\,\cos\alpha\cos 2\delta\right.\\ &+t_{21}^{Im}\,\frac{1}{2}\sqrt{\frac{5}{\pi}}\,\sin\alpha\cos 2\delta - t_{22}^{Re}\,\frac{1}{4}\sqrt{\frac{5}{\pi}}\,\cos 2\alpha\sin 2\delta\\ &\left.+t_{22}^{Im}\,\frac{1}{4}\sqrt{\frac{5}{\pi}}\,\sin 2\alpha\sin 2\delta\right)\hat{\boldsymbol{e}}_{\alpha}\\ &+\left(-t_{21}^{Re}\,\frac{1}{2}\sqrt{\frac{5}{\pi}}\,\sin\alpha\sin\delta - t_{21}^{Im}\,\frac{1}{2}\sqrt{\frac{5}{\pi}}\,\cos\alpha\sin\delta\right.\\ &+t_{22}^{Re}\,\frac{1}{2}\sqrt{\frac{5}{\pi}}\,\sin 2\alpha\cos\delta\\ &\left.+t_{22}^{Im}\,\frac{1}{2}\sqrt{\frac{5}{\pi}}\,\cos 2\alpha\cos\delta\right)\hat{\boldsymbol{e}}_{\delta}. \end{aligned} \tag{12}$$

The octopole ($\ell = 3$) vector spherical harmonics are

$$\begin{aligned}\boldsymbol{V}_{E3}(\alpha,\,\delta) = &\left(s_{31}^{Re}\,\frac{1}{8}\sqrt{\frac{7}{\pi}}\,\sin\alpha(5\sin^2\delta - 1)\right.\\ &+s_{31}^{Im}\,\frac{1}{8}\sqrt{\frac{7}{\pi}}\,\cos\alpha(5\sin^2\delta - 1)\\ &-s_{32}^{Re}\,\frac{1}{4}\sqrt{\frac{35}{2\pi}}\,\sin 2\alpha\sin 2\delta\\ &-s_{32}^{Im}\,\frac{1}{4}\sqrt{\frac{35}{2\pi}}\,\cos 2\alpha\sin 2\delta + s_{33}^{Re}\,\frac{1}{8}\sqrt{\frac{105}{\pi}}\,\sin 3\alpha\cos^2\delta\\ &\left.+\,s_{33}^{Im}\,\frac{1}{8}\sqrt{\frac{105}{\pi}}\,\cos 3\alpha\cos^2\delta\right)\hat{\boldsymbol{e}}_{\alpha}\\ &+\left(s_{30}\,\frac{1}{8}\sqrt{\frac{21}{\pi}}\,(5\sin^2\delta - 1)\cos\delta\right.\\ &+s_{31}^{Re}\,\frac{1}{8}\sqrt{\frac{7}{\pi}}\,\cos\alpha\sin\delta(15\sin^2\delta - 11)\\ &-s_{31}^{Im}\,\frac{1}{8}\sqrt{\frac{7}{\pi}}\,\sin\alpha\sin\delta(15\sin^2\delta - 11)\\ &-s_{32}^{Re}\,\frac{1}{4}\sqrt{\frac{35}{2\pi}}\,\cos 2\alpha\cos\delta(3\sin^2\delta - 1)\\ &+s_{32}^{Im}\,\frac{1}{4}\sqrt{\frac{35}{2\pi}}\,\sin 2\alpha\cos\delta(3\sin^2\delta - 1)\\ &+s_{33}^{Re}\,\frac{1}{8}\sqrt{\frac{105}{\pi}}\,\cos 3\alpha\cos^2\delta\sin\delta\\ &\left.-\,s_{33}^{Im}\,\frac{1}{8}\sqrt{\frac{105}{\pi}}\,\sin 3\alpha\cos^2\delta\sin\delta\right)\hat{\boldsymbol{e}}_{\delta} \end{aligned} \tag{13}$$

and

$$\begin{aligned}\boldsymbol{V}_{M3}(\alpha,\,\delta) = &\left(t_{30}\,\frac{1}{8}\sqrt{\frac{21}{\pi}}\,(5\sin^2\delta - 1)\cos\delta\right.\\ &+t_{31}^{Re}\,\frac{1}{8}\sqrt{\frac{7}{\pi}}\,\cos\alpha\sin\delta(15\sin^2\delta - 11)\\ &-t_{31}^{Im}\,\frac{1}{8}\sqrt{\frac{7}{\pi}}\,\sin\alpha\sin\delta(15\sin^2\delta - 11)\\ &-t_{32}^{Re}\,\frac{1}{4}\sqrt{\frac{35}{2\pi}}\,\cos 2\alpha\cos\delta(3\sin^2\delta - 1)\\ &+t_{32}^{Im}\,\frac{1}{4}\sqrt{\frac{35}{2\pi}}\,\sin 2\alpha\cos\delta(3\sin^2\delta - 1)\\ &+t_{33}^{Re}\,\frac{1}{8}\sqrt{\frac{105}{\pi}}\,\cos 3\alpha\cos^2\delta\sin\delta\\ &\left.-t_{33}^{Im}\,\frac{1}{8}\sqrt{\frac{105}{\pi}}\,\sin 3\alpha\cos^2\delta\sin\delta\right)\hat{\boldsymbol{e}}_{\alpha}\\ &+\left(-t_{31}^{Re}\,\frac{1}{8}\sqrt{\frac{7}{\pi}}\,\sin\alpha(5\sin^2\delta - 1)\right.\\ &-t_{31}^{Im}\,\frac{1}{8}\sqrt{\frac{7}{\pi}}\,\cos\alpha(5\sin^2\delta - 1)\\ &+t_{32}^{Re}\,\frac{1}{4}\sqrt{\frac{35}{2\pi}}\,\sin 2\alpha\sin 2\delta + t_{32}^{Im}\,\frac{1}{4}\sqrt{\frac{35}{2\pi}}\,\cos 2\alpha\sin 2\delta\\ &-\,t_{33}^{Re}\,\frac{1}{8}\sqrt{\frac{105}{\pi}}\,\sin 3\alpha\cos^2\delta\\ &\left.-t_{33}^{Im}\,\frac{1}{8}\sqrt{\frac{105}{\pi}}\,\cos 3\alpha\cos^2\delta\right)\hat{\boldsymbol{e}}_{\delta}. \end{aligned} \tag{14}$$

Appendix B
VLBA+*Gaia* Astrometry and Proper Motions

Table 6 lists the objects that show significant and consistent radio and optical proper motion. Based on the amplitudes of the proper motions, these are most likely intrinsic and associated with jets. Objects showing apparent superluminal motions are indicated in bold, as are the superluminal velocity components and amplitudes.

Table 7 lists the *Gaia* 2015.0 epoch J2000 coordinates, the VLBA-only and VLBA+*Gaia* proper motions obtained from the time series fits described in Section 3.2, and the *Gaia*-VLBA coordinate offset in *Gaia* standard deviations. The VLBA proper motions were obtained from bootstrap-resampled time series and may differ slightly from—but are

Table 6
Objects Showing Significant Consistent Radio and Optical Proper Motion

Name	VLBA+*Gaia* PM		Redshift	References[a]	D_M	Apparent Velocity		
	μ_α (μas yr^{-1})	μ_δ (μas yr^{-1})			(Mpc)	v_α (c)	v_δ (c)	$v_{\rm Total}$ (c)
0007+171	136.6(25.4)	−0.3(12.4)	1.60	1	4654	**10.1(1.9)**	−0.02(0.91)	**10.1(1.9)**
0016+731	−5.5(1.1)	5.1(0.7)	1.78	2	4969	−0.43(0.09)	0.40(0.06)	0.59(0.07)
0059+581	−7.5(0.4)	−2.8(0.5)	0.64	3	2359	−0.28(0.01)	−0.10(0.02)	0.30(0.02)
0119+041	−9.2(1.8)	6.0(1.9)	0.64	2	2359	−0.34(0.07)	0.22(0.07)	0.41(0.07)
0229+131	10.7(0.7)	7.0(0.7)	2.06	2	5409	0.92(0.06)	0.60(0.06)	**1.09(0.06)**
NRAO150	6.0(1.9)	16.6(2.3)	1.52	4	4505	0.43(0.14)	**1.18(0.16)**	**1.26(0.16)**
0420−014	−5.5(0.7)	−8.5(0.9)	0.92	2	3158	−0.27(0.03)	−0.42(0.04)	0.51(0.04)
NRAO190	−20.6(9.9)	−28.6(3.3)	0.84	2	2943	−0.96(0.46)	**−1.33(0.15)**	**1.64(0.30)**
0454−234	−3.8(0.7)	−7.1(0.8)	1.00	2	3365	−0.20(0.04)	−0.38(0.04)	0.43(0.04)
0458−020	−2.5(0.9)	−10.4(0.8)	2.29	2	5731	−0.23(0.08)	−0.94(0.07)	0.97(0.07)
0454+844	6.9(4.7)	19.7(3.0)	1.34	2	4145	0.45(0.31)	**1.29(0.20)**	**1.37(0.21)**
0552+398	0.2(0.4)	−3.5(0.4)	2.37	1	5835	0.02(0.04)	−0.32(0.04)	0.32(0.04)
0602+673	0.5(0.8)	20.4(1.2)	1.97	2	5274	0.04(0.07)	**1.70(0.10)**	**1.70(0.10)**
0657+172	7.2(1.4)	−5.4(1.9)	1.08	5	3562	0.41(0.08)	−0.30(0.11)	0.51(0.09)
0723−008	−50.0(6.5)	107.5(13.1)	0.13	1	542	−0.43(0.06)	0.92(0.11)	**1.02(0.10)**
0743+259	−3.5(2.8)	−33.4(3.6)	2.99	6	6543	−0.36(0.29)	**−3.46(0.37)**	**3.47(0.37)**
0805+410	5.4(1.1)	9.4(1.3)	1.42	2	4309	0.37(0.07)	0.64(0.09)	0.74(0.09)
1038+064	−15.1(3.5)	61.6(8.4)	1.27	2	3996	−0.95(0.22)	**3.89(0.53)**	**4.01(0.52)**
1045−188	22.3(4.3)	−73.5(10.4)	0.59	2	2202	0.78(0.15)	**−2.56(0.36)**	**2.67(0.35)**
1053+815	−7.1(1.4)	1.8(1.5)	0.71	3	2571	−0.29(0.06)	0.07(0.06)	0.30(0.06)
1057−797	0.5(1.3)	−7.5(1.2)	0.58	7	2170	0.02(0.04)	−0.26(0.04)	0.26(0.04)
1104−445	−20.1(3.0)	12.4(3.2)	1.60	2	4654	**−1.48(0.22)**	0.91(0.24)	**1.74(0.22)**
1124−186	1.7(1.1)	−6.8(1.2)	1.05	2	3489	0.09(0.06)	−0.38(0.07)	0.39(0.07)
1219+044	6.3(1.1)	−3.6(2.0)	0.97	2	3288	0.33(0.06)	−0.19(0.10)	0.38(0.07)
1300+580	5.2(0.7)	11.4(0.8)	1.09	2	3586	0.29(0.04)	0.65(0.05)	0.71(0.04)
1342+663	−40.9(7.3)	−9.8(2.8)	1.35	2	4166	**−2.69(0.48)**	−0.65(0.18)	**2.77(0.47)**
1424−418	−9.8(1.6)	2.0(1.8)	1.52	2	4505	−0.70(0.11)	0.14(0.13)	0.71(0.11)
1606+106	5.4(1.0)	0.1(0.9)	1.23	2	3908	0.32(0.06)	0.01(0.06)	0.32(0.06)
1622−253	−0.2(1.1)	8.0(1.4)	0.79	2	2803	−0.01(0.05)	0.35(0.06)	0.35(0.06)
1642+690	6.3(1.6)	−19.3(3.0)	0.75	2	2688	0.27(0.07)	−0.82(0.13)	0.86(0.12)
1657−562[b]	33.7(10.1)	−110.7(17.0)	…	…	…	…	…	…
NRAO530	7.4(1.3)	7.2(2.3)	0.90	2	3105	0.36(0.06)	0.35(0.11)	0.51(0.09)
1745+624	10.7(1.5)	10.4(2.2)	3.89	8	7328	**1.24(0.17)**	**1.21(0.25)**	**1.73(0.22)**
1846+322	−29.5(4.7)	7.2(5.9)	0.80	2	2831	**−1.32(0.21)**	0.32(0.26)	**1.36(0.21)**
3C395	66.2(9.9)	−32.1(6.9)	0.64	9	2359	**2.47(0.37)**	**−1.20(0.26)**	**2.74(0.35)**
1923+210[b]	10.0(2.4)	17.9(1.4)	…	…	…	…	…	…
1958−179	−7.7(1.0)	−4.0(1.4)	0.65	2	2390	−0.29(0.04)	−0.15(0.05)	0.33(0.04)
2007+777	22.8(3.0)	−0.0(1.5)	0.34	2	1350	0.49(0.06)	−0.00(0.03)	0.49(0.06)
3C418	−15.3(1.2)	−7.7(1.6)	1.69	10	4815	**−1.16(0.09)**	−0.59(0.12)	**1.30(0.10)**
2059+034	−5.3(3.5)	−25.0(3.8)	1.01	2	3390	−0.28(0.19)	**−1.34(0.20)**	**1.37(0.20)**
2126−158	−10.6(2.5)	−66.5(5.2)	3.27	2	6812	**−1.14(0.27)**	**−7.16(0.56)**	**7.25(0.55)**
2155−152	−30.4(6.3)	−40.1(7.3)	0.67	2	2451	**−1.18(0.24)**	**−1.55(0.28)**	**1.95(0.27)**
2209+236	21.7(2.0)	2.6(2.0)	1.13	2	3680	**1.26(0.12)**	0.15(0.12)	**1.27(0.12)**
2214+350	5.6(3.1)	−69.5(5.0)	0.51	1	1942	0.17(0.10)	**−2.13(0.15)**	**2.14(0.15)**
2229+695	39.3(3.3)	4.8(1.6)	1.41	2	4289	**2.67(0.22)**	0.33(0.11)	**2.69(0.22)**

Notes. Parenthetical values are 1σ uncertainties. Apparent velocities are in the rest frame of each object, in units of the speed of light, c (see Section 3.2). Bold type indicates the names and velocities of objects showing superluminal motion.

[a] Redshift references: (1) Wills & Wills (1976); (2) Healey et al. (2008); (3) Sowards-Emmerd et al. (2005); (4) Agudo et al. (2007); (5) Álvarez Crespo et al. (2016); (6) Hewett & Wild (2010); (7) Sbarufatti et al. (2009); (8) Hook et al. (1995); (9) Gelderman & Whittle (1994); (10) Smith & Spinrad (1980).

[b] 1657−562 and 1923+210 show VLBA+*Gaia* astrometric correspondence and significant proper motion, but the redshifts for these objects are unknown. If they have redshifts greater than 0.13 and 0.90, respectively, then their observed proper motions would be superluminal.

(This table is available in machine-readable form.)

Table 7
VLBA+*Gaia* Astrometry and Proper Motions

Name	*Gaia* 2015.0 Coordinates		VLBA PM		VLBA+*Gaia* PM		*Gaia*-VLBA Offset	
	R.A. (J2000) (h:m:s)	Decl. (J2000) (d:m:s)	μ_α (μas yr^{-1})	μ_δ (μas yr^{-1})	μ_α (μas yr^{-1})	μ_δ (μas yr^{-1})	$\Delta\alpha$ (σ)	$\Delta\delta$ (σ)
0002−478	00:04:35.65554(6)	−47:36:19.6040(8)	−23.1(13.2)	−46.5(20.0)	−22.9(13.2)	−47.4(19.8)	1.1	0.2
0003+380	00:05:57.17593(8)	+38:20:15.1435(4)	−15.4(9.9)	−1.5(11.3)	−12.6(9.2)	−18.9(13.6)	6.7	14.2
0003−066	00:06:13.89290(2)	−06:23:35.3351(1)	0.3(1.3)	3.7(1.8)	0.4(1.3)	3.5(1.8)	0.4	1.4
IIIZW2	00:10:31.00592(2)	+10:58:29.5038(2)	2.3(12.3)	−9.7(11.8)	3.3(11.5)	−13.1(12.0)	0.9	2.2
0007+171	00:10:33.99072(4)	+17:24:18.7609(3)	136.2(27.2)	9.8(14.7)	136.6(25.4)	−0.3(12.4)	0.6	2.0

Note. The *Gaia* coordinates are for epoch 2015.0, expressed in the J2000 reference frame. The *Gaia*-VLBA offsets are expressed in standard deviations of the *Gaia* astrometry from the VLBA time series fit, assuming that the error is dominated by the sole *Gaia* epoch in each coordinate.

(This table is available in its entirety in machine-readable form.)

statistically consistent with—the Truebenbach & Darling (2017) proper motion catalog. The VLBA+*Gaia* proper motion catalog in Table 7 forms a subset of the VLBA-only Truebenbach & Darling (2017) catalog because not all radio sources have *Gaia* counterparts.

ORCID iDs

Jeremy Darling https://orcid.org/0000-0003-2511-2060

References

Agudo, I., Bach, U., Krichbaum, T. P., et al. 2007, A&A, 476, L17
Álvarez Crespo, N., Massaro, F., Milisavljevic, D., et al. 2016, AJ, 151, 95
Arzoumanian, Z., Brazier, A., Burke-Spolaor, S., et al. 2016, ApJ, 821, 13
Biretta, J. A., Sparks, W. B., & Macchetto, F. 1999, ApJ, 520, 621
Blandford, R. D., McKee, C. F., & Rees, M. J. 1977, Natur, 267, 211
Bond, J. R., Jaffe, A. H., & Knox, L. 1998, PhRvD, 57, 2117
Book, L. G., & Flanagan, É. É. 2011, PhRvD, 83, 024024
Bower, G. C., Demorest, P., Braatz, J., et al. 2015, arXiv:1510.06432
Braginsky, V. B., Kardashev, N. S., Polnarev, A. G., & Novikov, I. D. 1990, NCimB, 105, 1141
Cohen, M. H., Kellermann, K. I., Shaffer, D. B., et al. 1977, Natur, 268, 405
Gaia Collaboration, Brown, A. G. A., Vallenari, A., et al. 2016a, A&A, 595, A2
Gaia Collaboration, Prusti, T., de Bruijne, J. H. J., et al. 2016b, A&A, 595, A1
Gelderman, R., & Whittle, M. 1994, ApJS, 91, 491
Gwinn, C. R., Eubanks, T. M., Pyne, T., Birkinshaw, M., & Matsakis, D. N. 1997, ApJ, 485, 87
Healey, S. E., Romani, R. W., Cotter, G., et al. 2008, ApJS, 175, 97
Hewett, P. C., & Wild, V. 2010, MNRAS, 405, 2302
Hogg, D. W. 1999, arXiv:astro-ph/9905116
Hook, I. M., McMahon, R. G., Patnaik, A. R., et al. 1995, MNRAS, 273, L63
Ishino, H., Akiba, Y., Arnold, K., et al. 2016, Proc. SPIE, 9904, 99040X
Kaiser, N., & Jaffe, A. 1997, ApJ, 484, 545
Kamionkowski, M., Kosowsky, A., & Stebbins, A. 1997, PhRvL, 78, 2058
Kovalev, Y. Y., Petrov, L., & Plavin, A. V. 2016, A&A, 598, L1
Meyer, E. T., Georganopoulos, M., Sparks, W. B., et al. 2015, Natur, 521, 495
Mignard, F., & Klioner, S. 2012, A&A, 547, A59
Mignard, F., Klioner, S., Lindegren, L., et al. 2016, A&A, 595, A5
Newville, M., Stensitzki, T., Allen, D. B., & Ingargiola, A. 2014, LMFIT: Non-Linear Least-Square Minimization and Curve-Fitting for Python, Zenodo, doi:10.5281/zenodo.11813
Paine, J., Darling, J., & Truebenbach, A. E. 2018, ApJS, 236, 37
Petrov, L., & Kovalev, Y. Y. 2017, MNRAS, 467, L71
Reid, M. J., Menten, K. M., Brunthaler, A., et al. 2014, ApJ, 783, 130
Robin, A. C., Luri, X., Reylé, C., et al. 2012, A&A, 543, A100
Sbarufatti, B., Ciprini, S., Kotilainen, J., et al. 2009, AJ, 137, 337
Seljak, U., & Zaldarriaga, M. 1997, PhRvL, 78, 2054
Sivia, D. S., & Skilling, J. 2006, Data Analysis: A Bayesian Tutorial (2nd ed.; Oxford: Oxford Univ. Press)
Smith, H. E., & Spinrad, H. 1980, ApJ, 236, 419
Smith, T. L., Pierpaoli, E., & Kamionkowski, M. 2006, PhRvL, 97, 021301
Sowards-Emmerd, D., Romani, R. W., Michelson, P. F., Healey, S. E., & Nolan, P. L. 2005, ApJ, 626, 95
Thorne, K. S. 1980, RvMP, 52, 299
Titov, O., & Lambert, S. 2013, A&A, 559, A95
Titov, O., Lambert, S. B., & Gontier, A.-M. 2011, A&A, 529, A91
Truebenbach, A. E., & Darling, J. 2017, ApJS, 233, 3
Wills, D., & Wills, B. J. 1976, ApJS, 31, 143
Xu, M. H., Wang, G. L., & Zhao, M. 2013, MNRAS, 430, 2633